Available online at www.sciencedirect.com
ScienceDirect
Journal of Magnetic Resonance 182 (2006) 160–167
JMR Journal of Magnetic Resonance
www.elsevier.com/locate/jmr

Potential advantage of higher-order modes of birdcage coil for parallel imaging

Chunsheng Wang, Peng Qu, Gary X. Shen *

MRI Lab, Department of Electrical and Electronic Engineering, The University of Hong Kong, Hong Kong, PR China

Received 14 February 2006; revised 13 June 2006
Available online 10 July 2006

Abstract

The potential advantages of the higher-order resonant modes of a low-pass birdcage coil for parallel imaging are investigated using FDTD simulations in a spherical phantom. Better parallel imaging performance can be achieved in axial planes than in sagittal planes. If more modes are employed, the average *g*-factor (g_{mean}) and maximum *g*-factor (g_{max}) will be improved for a specific acceleration factor (R). *G*-factor performance at 3 T ($g_{mean} = 1.79$, $g_{max} = 3.55$) and 7 T ($g_{mean} = 1.60$, $g_{max} = 2.45$) can be achieved even with an acceleration factor as high as four when all six order modes of 12-rung low-pass birdcage coil are incorporated for imaging on a mid-axial plane. For a specific number of channels, the optimum combination of corresponding modes can be obtained for different acceleration factors. Based on the *g*-factor and SNR performance, the total degenerate multi-mode birdcage coil with six order resonant modes has better homogeneous coverage and SENSE performance than the 8-element phased array coil, although requiring fewer channels. In addition, the dielectric effects at high field can improve the parallel imaging performance.

Keywords: Birdcage coil; FDTD; Higher-order modes; Parallel MRI; *G*-factor

1. Introduction

In parallel imaging methods, such as sensitivity encoding (SENSE) [1] and simultaneous acquisition of spatial harmonics (SMASH) [2], signals from multiple surface coils are acquired simultaneously to reduce acquisition time dramatically without significant sacrifices in spatial resolution or signal-to-noise ratio (SNR). These methods capitalize on the different spatial sensitivity of each array element for spatial encoding. The drawback of using surface coils is that the sensitivity of a surface coil decreases with depth into the human tissue. Sometimes, homogeneous coverage of volume coils, such as birdcage coil [3], TEM coil [4] and microstrip volume coil [5], is preferred in clinical applications. However, the excellent homogeneity of their operational mode can not provide the additional spatial information needed for SENSE and SMASH reconstruction. The higher-order modes of the volume coils have different sensitivity magnitude and phase profiles from the uniform mode. These different sensitivity profiles of each mode can be used for parallel imaging.

Generally, there are N/2 resonant frequencies for an N-rung low-pass birdcage coil [3]. Each resonant frequency is related with two orthogonal degenerate modes, which are defined as the same order mode in this work. Therefore there are N/2 order modes for an N-rung low-pass birdcage coil. A standing wave in the low-frequency mode (first mode) generates currents in straight segments proportional to cosine function of the cylindrical coordinate azimuthal angle, which can produce a homogeneous RF magnetic field ($\mathbf{B}_1$) inside the coil. Higher-order modes produce increasingly less homogeneous B_1 field as the number of order increases. Therefore, the first mode of the low pass birdcage coil is mostly used in common MRI applications. Actually the higher-order modes of a birdcage coil also can be used for MR imaging. Sprenger demonstrated that the

* Corresponding author.
E-mail address: gxshen@eee.hku.hk (G.X. Shen).

1090-7807/$ - see front matter © 2006 Elsevier Inc. All rights reserved.
doi:10.1016/j.jmr.2006.06.015

second mode of low-pass birdcage has a characteristic similar to a "wrap around" surface coil [6]. The B_1 field magnitude of second mode is proportional to the radius. In addition, the second order does not couple to the center of the subjects, so it has higher SNR at the periphery of the subject than the first order of the birdcage. Wong also proposed a method which can simultaneously acquire data in both the first mode and the second mode of an 8-rung low-pass birdcage coil at the same frequency, and a gain of 10–40% in SNR was achieved around the periphery of the sample [7].

If the birdcage coil is totally degenerate, all the modes can be resonant at the same frequency. Lesser rendered an 8-rung bandpass birdcage coil degenerate and used it as a phased array [8]. Due to spatially different sensitivity profiles of each mode, these modes have potential for parallel imaging. The standard homogeneous mode (first mode) and the first gradient mode (second mode) of an eight-rung low pass birdcage coil have been applied for SENSE imaging at 1.5 T successfully [9], and 2-fold acceleration was achieved with the average g-factor of 1.55.

In this study, the potential advantage of using higher-order modes of a 12-rung low-pass birdcage coil for parallel imaging is investigated at 3 and 7 T. Since more modes are employed, the improved performance of parallel imaging is expected.

2. Methods

The finite difference time domain (FDTD) method is normally used to solve for electromagnetic fields which interact with objects with irregular geometries [10]. This method can deal with difficult issues of non-regular boundary condition with high accuracy [11]. Here, the FDTD method was used to calculate electrical and magnetic fields in samples (sensitivity profile of each resonant mode) through time-dependent Maxwell's curl equations at the resonant frequencies of 128 and 300 MHz,

$$\nabla \times \mathbf{E} = -\partial \mathbf{B}/\partial t, \tag{1}$$

$$\nabla \times \mathbf{H} = \partial \mathbf{D}/\partial t + \sigma \mathbf{E}, \tag{2}$$

where $\mathbf{E}$ and $\mathbf{H}$ are the electric and magnetic field intensities. $\mathbf{B}$, $\mathbf{D}$ and σ refer, respectively, to the magnetic flux density, the electric flux density and electric conductivity. All electromagnetic fields were calculated by using the commercially available software XFDTD (Recmom, Inc., State College, PA), whereas the post-processing of the electromagnetic field data for calculating circularly polarized component of the RF magnetic field ($\mathbf{B}_1$) were performed by using home-made MATLAB program. To minimize the errors caused by stair stepping, the Yee cells, which are the basic elements of 3D meshes in FDTD method, were chosen as 2 mm in each dimension to fully characterize the structure of the coils. A region of interest (ROI), $26 \times 26 \times 28$ cm^3 is divided into a mesh of 2,366,000 Yee cells. Based on the Courant stability condition, the time step should satisfy Eq. (3) for cubical cells:

$$\Delta t \leqslant (\Delta x)/(c\sqrt{3}), \tag{3}$$

where Δt, Δx and c are time step, Yee cell side dimension and light speed in free space respectively. Here, the time step was 3.85 ps as the tradeoff between accuracy and computation time. The simulation was run for 100,000 steps to ensure that the steady state was reached. The Liao boundary condition [12] was used for the outer boundary truncation of the grid. A 12-rung low-pass birdcage coil (20-cm i.d. and 21-cm length) was modeled in the ROI. The conductivity of copper (5.95×10^7 S/m) was assigned to the coil cells. The phantom was modeled by a sphere with 18 cm diameter (relative permittivity $\varepsilon_r = 63.025$, conductivity $\sigma = 0.464$ S/m at 128 MHz and $\varepsilon_r = 51.898$, $\sigma = 0.553$ S/m at 300 MHz) which mimics the average brain tissue [13]. Voltage sources has been used to model capacitors [14,15] and it has proved accurate up to 128 MHz for a bandpass birdcage coil [15]. Here, voltage sources were placed at each rung to model capacitors and driving ports. To decrease the electrical length of unbroken conductors in calculation at 300 MHz (7 T), every two additional voltage sources are placed on both sides of each rung, which are close to the end-rings (about 1 cm). In other words, each rung contains three voltage sources with the same amplitude and phase for 7 T calculation. The modeled coil and sample for 3 T calculations are illustrated in Fig. 1.

It is assumed that the signal is received in quadrature for every order mode (or two orthogonal degenerate modes). Then the sensitivity profile of each order mode can be

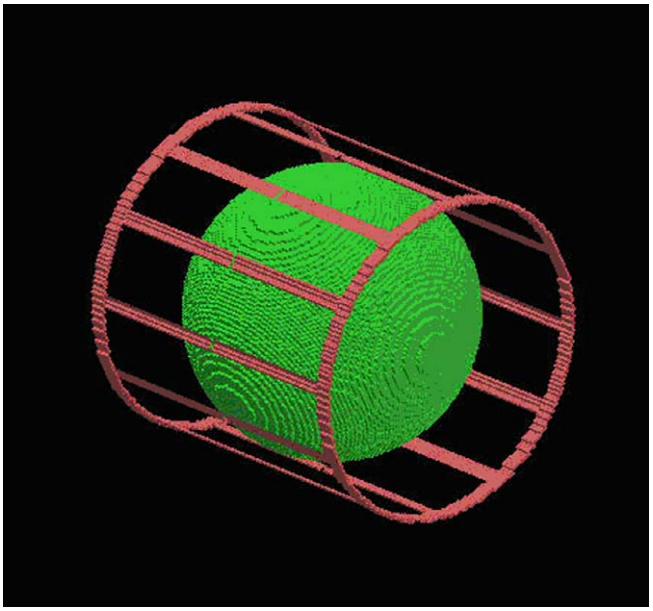

Fig. 1. A 12-rung (20-cm i.d., 21-cm length) low-pass birdcage coil are modeled in XFDTD. The driving voltage source is placed at the middle of each rung. The phantom having electric properties of average brain tissue is an 18 cm diameter sphere.

Table 1
The initial phases (in degree) of each voltage source for each order mode

Voltage source	1	2	3	4	5	6	7	8	9	10	11	12
1st Mode	0	30	60	90	120	150	180	210	240	270	300	330
2nd Mode	0	60	120	180	240	300	0	60	120	180	240	300
3rd Mode	0	90	180	270	0	90	180	270	0	90	180	270
4th Mode	0	120	240	0	120	240	0	120	240	0	120	240
5th Mode	0	150	300	90	240	30	180	330	120	270	60	210
6th Mode	0	180	0	180	0	180	0	180	0	180	0	180

estimated by driving the loaded coil in quadrature with the specific voltage sources setting. In particular, all the voltage sources have the same unit amplitude, and the initial phases of each voltage source for each order mode are given by

$$\theta_{m,n} = \frac{360}{N} m(n-1), \tag{4}$$

where N is the number of rungs in the low-pass birdcage, $\theta_{m,n}$ (in degree) is the initial phase of the voltage source in the nth rung ($1 \leqslant n \leqslant N$) for the mth order mode ($1 \leqslant m \leqslant N/2$). In this work, $N = 12$ and the phases of each voltage source for each order mode at the initial time are set as in Table 1.

Then the phases of voltage sources at the first mode ($m = 1$) are the cylindrical coordinate azimuthal angles. For the highest order mode ($m = 6$), the adjacent rungs have currents equal in magnitude but of opposite phase.

The positive ($\mathbf{B}_1^+$) and negative ($\mathbf{B}_1^-$) circularly polarized magnetic field component were calculated as [16].

$$\mathbf{B}_1^+ = \frac{\mathbf{B}_{1x} + i\mathbf{B}_{1y}}{2}, \tag{5}$$

$$\mathbf{B}_1^- = \frac{(\mathbf{B}_{1x} - i\mathbf{B}_{1y})^*}{2}, \tag{6}$$

where $\mathbf{B}_{1x}$ and $\mathbf{B}_{1y}$ are x- and y-oriented RF magnetic fields created by the coil driven in quadrature. Here, i is the imaginary unit and their imaginary components are 90° out of phase in time with real ones. The asterisk denotes a complex conjugate. $\mathbf{B}_1^+$ is assumed as the component that rotates in the same direction as the nuclei. $(\mathbf{B}_1^-)^*$can be taken as sensitivity of the coils by the principle of reciprocity [16]. Here, the $(\mathbf{B}_1^-)^*$ fields of each mode are calculated

Table 2
Average g-factors (g_{mean}) and maximum g-factors (g_{max}) of different acceleration factors ($R = 2$, 3, 4, 5, and 6) by using different modes combinations for imaging on the mid-axial plane at 3 T

R	Modes	(1,2)	(1,2,3)	(1,2,3,4)	(1,2,3,4,5)	(1,2,3,4,5,6)
2	g_{mean}	1.2549	1.0830	1.0372	1.0289	1.0285
	g_{max}	2.4629	1.4491	1.1414	1.0836	1.1173
3	g_{mean}		1.8022	1.3457	1.2196	1.1880
	g_{max}		5.2836	2.4667	1.6320	1.5625
4	g_{mean}			3.1427	1.9931	1.7978
	g_{max}			12.1212	5.1846	3.5531
5	g_{mean}				5.6930	4.1331
	g_{max}				34.7194	15.5743
6	g_{mean}					9.1728
	g_{max}					64.4726

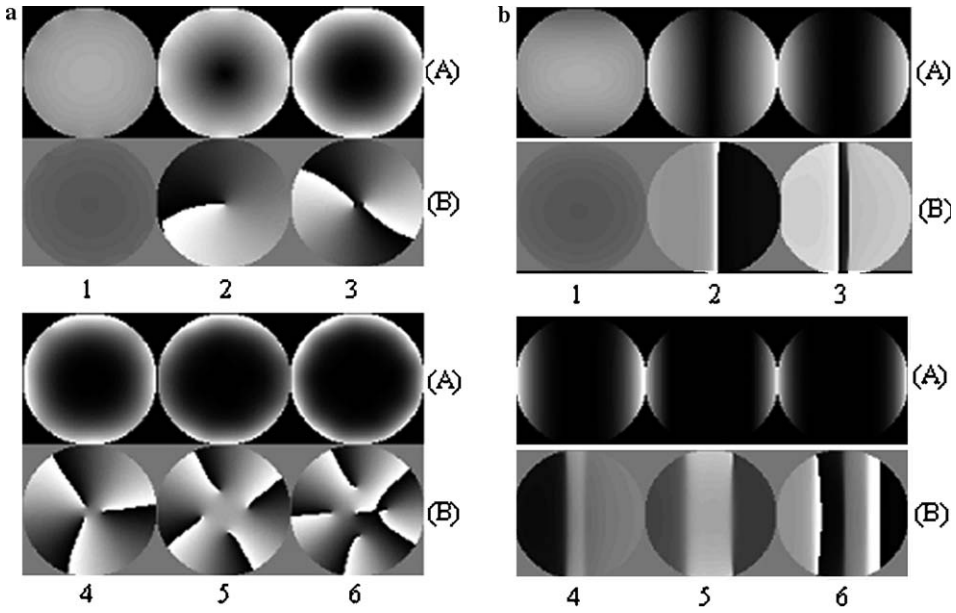

Fig. 2. Magnitude of $(\vec{B}_1^-)^*$ fields (shown in A row and normalized) and phase of $(\vec{B}_1^-)^*$ fields (shown in B row, range from $-\pi$ to π) for six order modes of the 12-rung low-pass birdcage coil at 3 T. (a) the mid-axial plane (b) the mid-sagittal plane.

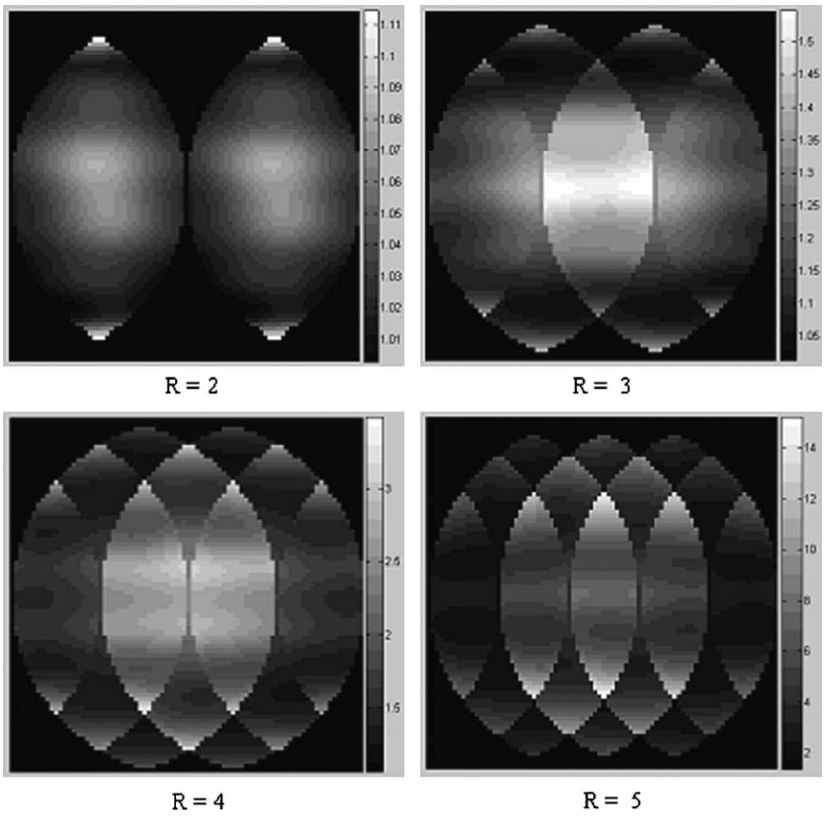

Fig. 3. Geometry factor maps of different acceleration factors ($R = 2$, 3, 4 and 5) with all six order modes employed for imaging on the mid-axial plane. SENSE direction was transverse. Color bar gives numerical values associated with gray shades.

from two sets of transient $\mathbf{B}_1$ fields (calculated by FDTD method) which are a quarter period apart in time.

Geometry factor (g-factor) describes the ability with a given coil configuration to separate pixels superimposed by aliasing, and it is regarded as an important criterion for the design of RF coils for parallel MRI. Generally, the less the g-factor is, the better parallel imaging performance the coil has. G-factor is always at least equal to one and can be calculated through Eq. (7) [1]:

$$g_\rho = \sqrt{\left((S^H\psi^{-1}S)^{-1}\right)_{\rho,\rho}(S^H\psi^{-1}S)_{\rho,\rho}} \geqslant 1, \tag{7}$$

where $\mathbf{S}$ is the reformatted coil sensitivity matrix, ρ is the index of the voxel within the set of voxels to be separated; and $\mathbf{S}^{\mathrm{H}}$ denotes the transposed complex conjugate operation. Here, the receive noise correlation matrix Ψ was approximated by pairwise summing the scalar products of the sensitivities over N equidistant locations within the sample [17];

$$\psi_{\gamma,\gamma'} = \sum_{i=1}^{N} B_\gamma(r_i)\cdot B_{\gamma'}(r_i), \tag{8}$$

where r_i denotes the position of the pixel i and B_γ denotes the spatial sensitivity of the coil γ. The geometry-related noise enhancement with respect to full Fourier encoding is:

$$N_{\mathrm{SENSE},\rho} = N_{\mathrm{full},\rho}\cdot g_\rho \cdot \sqrt{R}, \tag{9}$$

where

$$N_{\mathrm{full},\rho} = (\sqrt{(S^H\psi^{-1}S)_{\rho,\rho}})^{-1}. \tag{10}$$

Generally, SENSE method incurs a loss in SNR due to both reduced imaging time (acceleration factor, R) and coil geometry (g-factor) [18]. The SNR for accelerated parallel imaging using the SENSE method can be calculated as

$$\mathrm{SNR}_{\mathrm{SENSE}} = \frac{\mathrm{SNR}_{\mathrm{opt}}}{g\sqrt{R}}, \tag{11}$$

where g is g-factor, R is acceleration factor and SNR_{opt} is the SNR for B_1 weighted optimum phased array combining [19]. The spatially varying g-factor represents the loss in SNR due to ill-conditioning of the matrix inverse, which depends on the acceleration rate, the number of coils (or modes of one coil), specific coil sensitivity profiles, slice orientation and phase encoding direction.

3. Results and discussion

3.1. Evaluation of higher-order modes of birdcage coil at 3 T

The $(\vec{B}_1^-)^*$ field magnitude and phase distributions of the 12-rung low-pass birdcage coil's six order resonant modes are illustrated in Fig. 2 when we assume all modes are resonant at the same frequency (128 MHz).

The $(B_1^-)^*$ field magnitude distribution of the first mode is much more homogeneous than those of other order

resonant modes. And the higher-order modes produce increasingly less homogeneous $(\bar{B_1^-})^*$ field as the number of order increases. However, the higher order modes have higher sensitivity at the periphery of the spherical phantom than the first order mode. The phase distribution of each mode is also different, which may provide benefits for parallel imaging.

The mean g-factors (g_{mean}) and maximum g-factors (g_{max}) by using different modes combinations for imaging on the mid-axial plane are listed in Table 2. It is shown that when more modes are employed, the average g-factor and maximum g-factor will decrease for a fixed acceleration factor.

When all six order modes are employed for parallel imaging, the geometry factor maps (g-factor map) at different acceleration rates are shown in Fig. 3 (mid-axial) and Fig. 4 (mid-sagittal), and the corresponding detailed information about the g-factor maps are listed in the Table 2 (last column) and Table 3, respectively.

Because of the symmetry of the birdcage coil, the SENSE-encoding direction can be any direction on the axial plan for axial imaging. For imaging on a sagittal plane, SENSE direction can be along longitudinal direction besides transverse directions. Here, we set SENSE direction as transverse for the axial plane and the sagittal plan.

According to Figs. 3 and 4, the distinct bright areas (with high g-factors) lie in the center of the folded FOV, reflecting unfavorable sensitivity relations. Note that in these maps the object borders are reflected by characteristic contours due to the exclusion of pixels outside the sample. For imaging on the mid-axial plane, the average g-factor is still less than 1.8 and maximum g-factor is about 3.55 even the acceleration factor up to four when all six order resonant modes are used. If $R > 4$, the g-factor increases dramatically. In Ref. [20], while eight rectangular loops were positioned on a cylinder in simulation, the average g-factor is 6.11 for an acceleration factor of 4 within a head-sized phantom. It is much higher than the g_{mean} of 1.79 obtained in this work. This demonstrates that the six order resonant modes may have better SENSE performance than the 8-element phased array coil, although requiring fewer channels.

For imaging on the mid-sagittal plane, the g-factor performance is much worse than imaging on the mid-axial plane. Even if the acceleration ratio is 2, the average g-factor of imaging on the mid-sagittal plane is 2.73 and the

Table 3
Average and maximum g-factor for different acceleration factors ($R = 2$, 3, 4 and 5) with all six order modes employed for imaging on the mid-sagittal plane (several exceptional points were removed) at 3 T

Acceleration factor (R)	2	3	4	5
Average g-factor	2.726	12.859	27.386	63.873
Maximum g-factor	17.959	34.443	452.314	987.621

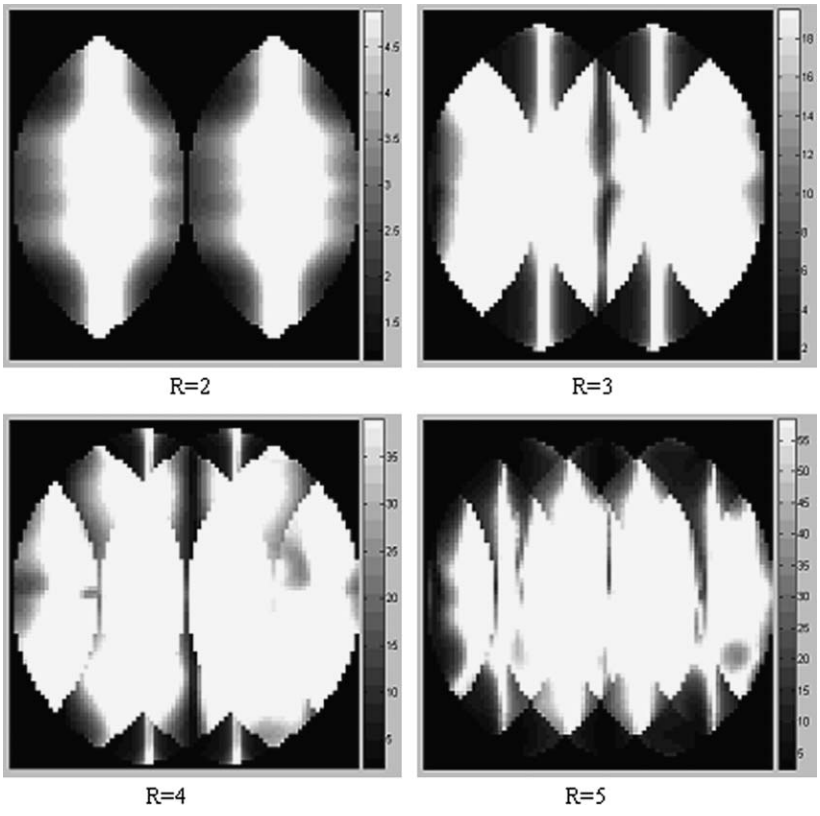

Fig. 4. Geometry factor maps of different acceleration factors ($R = 2$, 3, 4 and 5) with all six order modes employed for imaging on the mid-sagittal plane. SENSE direction was transverse. Color bar gives numerical values associated with gray shades. Values above maximum value in scale are represented with the same (white) color.

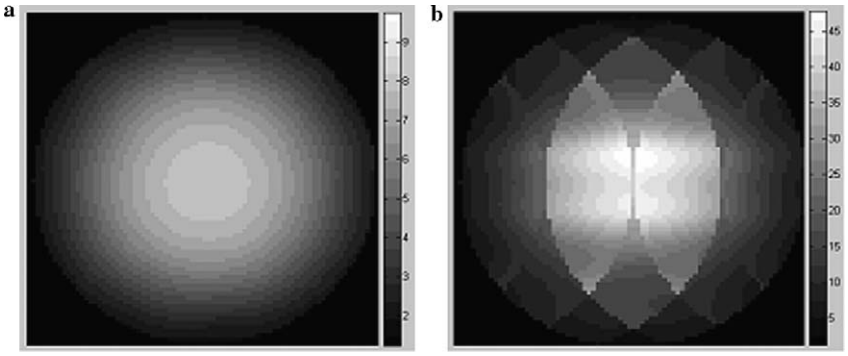

Fig. 5. Noise maps in the mid-axial plane. (a) The noise distribution for full Fourier encoding N_{full} (b) The geometry-related total noise distribution for SENSE with $R = 4$ (N_{SENSE}).

maximum g-factor is about 18. This is mainly caused by the small difference of magnitude and phase of $(B_1^-)^*$ fields on the mid-sagittal plane between each mode. On the mid-sagittal plane, the $(B_1^-)^*$ field magnitudes at the center of each mode are small (shown in black in Fig. 2(b)) and close to each other except for the first mode, and the difference of $(B_1^-)^*$ field phases is also limited. It is one of the reasons that the bright lines exist in g-factor maps on the mid-sagittal plan (Fig. 4). On the mid-axial plane, although the $(B_1^-)^*$ field magnitude between each mode is similar, the phase of each mode is much different. This characteristic well satisfies the requirement of signal separation. It illustrates the key role of phase in sensitivity encoding [17,21] and is the important reason for better g-factor performance of imaging on the mid-axial plane.

The basic noise maps N_{full} derived from Eq. (10) and the geometry-related total noise N_{SENSE} derived from Eq. (9) with $R8 = 4$ in the mid-axial plane are illustrated in Fig. 5. The noise is given in arbitrary units. Compared with the noise for full Fourier encoding, the total noise of SENSE ($R = 4$) is enhanced by a factor of 3.6 on the overall axial-plane within the sample according to Eq. (9) when $g_{\text{mean}} = 1.8$ and $R = 4$. The region with high noise level is still located at the center of the sample.

The SNR for full Fourier encoding is inversely proportional to N_{full}. It was calculated and shown in Fig. 6. Compared with the Fig. 4 ($n = 8$) in the Ref. [20], the relative homogeneous coverage is also better.

In practice, the number of receive channels of a MRI system is limited. To find out optimal mode combinations for a specific number of receive channels, we select different combinations of four modes out of all the six order resonant modes to calculate g-factors for different acceleration factors. Here, imaging on the mid-axial plane is selected for calculating g-factors because it has better performance than imaging on the mid-sagittal plane. The results are shown in Table 4.

For different acceleration factors (R), the optimum choice of mode combination may be different. When $R = 2$, the combination of modes (1, 2, 3 and 4) has the lowest average g-factor ($g_{\text{mean}} = 1.0372$). When $R = 3$, the combination of modes (1, 2, 3 and 5) has slightly smaller average g-factor than the combination of modes (1, 2, 3 and 4), and it has much lower maximum g-factor ($g_{\max} = 1.9369$) than combination of modes 1, 2, 3 and 4 ($g_{\max} = 2.3965$). For $R = 4$, the combination of modes (1,

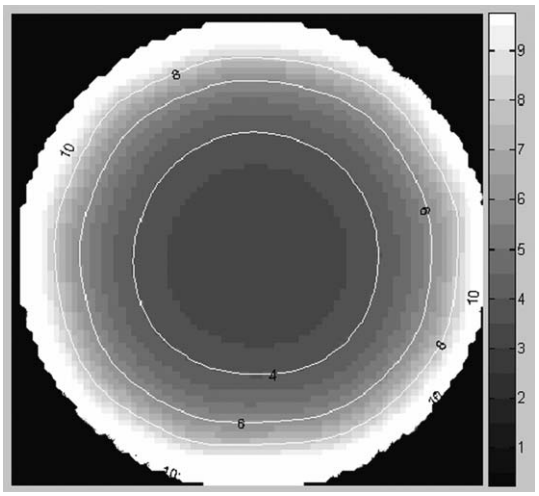

Fig. 6. Normalized SNR distribution for full Fourier encoding.

Table 4
Average and maximum g-factors of different acceleration factors ($R = 2$, 3 and 4) by selecting four modes out of all six order modes for imaging on the mid-axial plane at 3 T

Modes	$R = 2$		$R = 3$		$R = 4$	
	g_{mean}	$g_{\max}$	g_{mean}	$g_{\max}$	g_{mean}	$g_{\max}$
(1,2,3,4)	1.0372	1.1414	1.3457	2.4667	3.1427	12.121
(1,2,3,5)	1.0480	1.1086	1.3334	1.9369	2.8492	62.581
(1,2,3,6)	1.0578	1.1914	1.3888	2.6105	2.9106	71.037
(1,2,4,5)	1.0707	1.2334	1.3537	2.8562	2.2955	10.241
(1,2,4,6)	1.0663	1.2007	1.4606	20.7085	3.6308	88.154
(1,2,5,6)	1.1367	1.5593	1.5431	3.0565	2.8780	20.588
(1,3,4,5)	1.1346	2.3669	1.4227	8.3733	3.3654	130.908
(1,3,4,6)	1.1316	2.3536	1.4540	7.7298	3.5835	98.807
(1,3,5,6)	1.2247	12.1061	1.7677	42.7057	3.6344	157.489
(1,4,5,6)	1.2649	2.8783	1.9716	12.1952	6.1652	288.914
(2,3,4,5)	1.0636	1.3055	1.4715	2.4898	3.1381	16.115
(2,3,4,6)	1.0679	1.1982	1.4398	2.4419	3.2418	67.575
(2,3,5,6)	1.1125	1.3902	1.5254	4.2813	2.9159	43.606
(2,4,5,6)	1.2336	3.7971	1.7428	13.2582	5.6199	246.793
(3,4,5,6)	1.0830	1.3464	1.5562	6.9606	5.8684	48.871

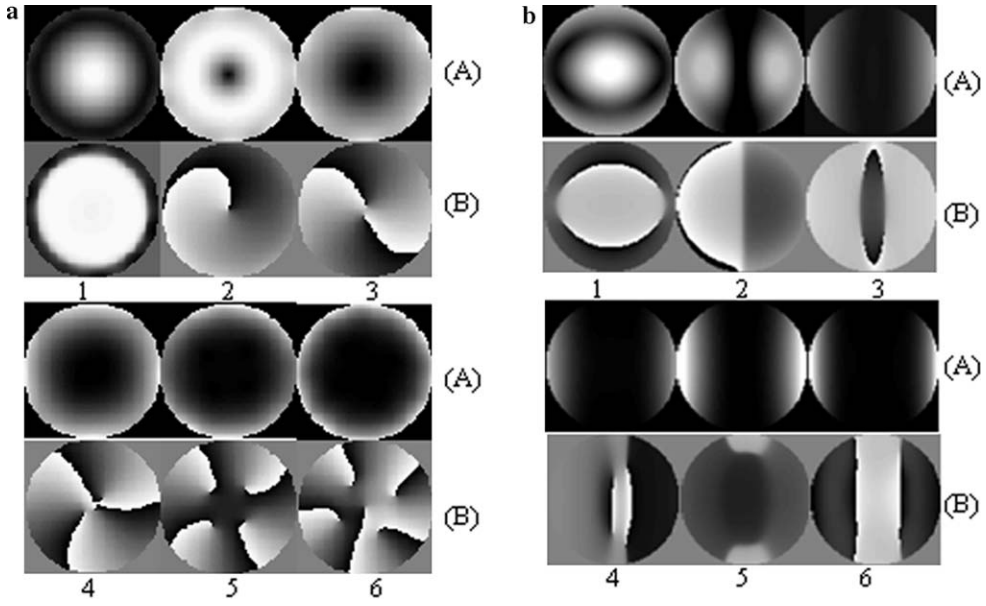

Fig. 7. Magnitude of $(\vec{B}_1^-)^*$ fields (shown in A row and normalized) and phase of $(\vec{B}_1^-)^*$ fields (shown in B row, range from $-\pi$ to π) for six order modes of the 12-rung low-pass birdcage coil at 7 T. (a) the mid-axial plane (b) the mid-sagittal plane.

2, 4 and 5) has better g-factor performance ($g_{mean} = 2.2955$, $g_{max} = 10.241$) than others. The optimal mode combinations for other number of receive channels can be calculated in the same way.

3.2. Evaluation of higher-order modes of birdcage coil at 7 T

The $(\vec{B}_1^-)^*$ field magnitude and phase distributions of the 12-rung low-pass birdcage coil's six order resonant modes at 7 T are illustrated in Fig. 7.

Compared with $(\vec{B}_1^-)^*$ field magnitude and phase distribution at 3 T, the $(\vec{B}_1^-)^*$ field magnitude and phase distributions at 7 T show stronger dielectric resonance effect.

When all six order modes are employed for parallel imaging at 7 T, the average and the maximum g-factor for different acceleration factors ($R = 2$, 3, 4 and 5) on the mid-axial plane and the mid-sagittal plane are listed in Table 5.

The average g-factors and maximum g-factors for 7 T are remarkably less than those for 3 T. It is shown that the dielectric effects can decrease the g-factor and increase the parallel imaging performance at ultra high field.

Table 5
Average g-factor (g_{mean}) and maximum g-factor (g_{max}) for different acceleration factors (R) with all six order modes employed for imaging on the mid-axial plane and mid-sagittal plane (several exceptional points were removed) at 7 T

	R	2	3	4	5
Mid-axial plane	g_{mean}	1.0150	1.1191	1.6021	3.1376
	g_{max}	1.2216	1.9402	2.4488	10.0886
Mid-sagittal plane	g_{mean}	1.8011	7.7103	20.3302	63.8728
	g_{max}	12.9374	33.4723	310.1126	849.4637

So, there are some advantages of using higher-order resonant modes of birdcage coil for parallel imaging, such as the available higher acceleration factor, arbitrary SENSE direction on axial plane, especially the better homogeneous coverage and high SNR at periphery of sample etc. But it is still a challenge to implement such a totally degenerate birdcage coil for SENSE imaging, because it is extremely difficult to tune all resonant modes into same frequency and receive signal of each channel individually with any currently used techniques.

4. Conclusions

The potential advantages of higher-order resonant modes of birdcage coil for parallel imaging is investigated by evaluating geometric factors and SNR. Based on g-factor comparison, imaging on a mid-axial plane has much better parallel imaging performance than imaging on a mid-sagittal plane. The average g-factor is still less than 1.8 and the maximum g-factor is less than 3.6 even if the acceleration factor is as high as four when all six order resonant modes of a 12-rung low-pass birdcage coil are incorporated for imaging on a mid-axial plane at 3 T. Considering the limitation of the number of channels in MRI system, the optimized combination of corresponding modes can be obtained based on different acceleration factors. Based on the g-factor and SNR performance, the total degenerate multi-mode birdcage coil with six order resonant modes has better homogeneous coverage and SENSE performance than the 8-element phased array coil, while requiring fewer channels. In addition, the dielectric effects at high field can improve the parallel imaging performance according to the g-factors evaluation at 3 and 7 T.

References

[1] K.P. Pruessmann, M. Weiger, M.B. Scheidegger, P. Boesiger, SENSE: sensitivity endcoding for fast MRI, Magn. Reson. Med. 42 (1999) 952–962.

[2] D.K. Sodickson, W.J. Manning, Simultaneous acquisition of spatial harmonics (SMASH): fast imaging with radiofrequency coil arrays, Magn. Reson. Med. 38 (1997) 591–603.

[3] C.E. Hayes, W.A. Edelstein, J.F. Schenck, et al., An efficient, highly homogeneous radiofrequency coil for whole-body NMR imaging at 1.5T, J. Magn. Reson. 63 (1985) 622–628.

[4] J.T. Vaughan, H.P. Hetherington, J.G. Harrison, J.O. Out, J.W. Pan, G.M. Pohost, High frequency volume coils for clinical NMR imaging and spectroscopy, Magn. Reson. Med. 32 (1994) 206–218.

[5] X. Zhang, K. Ugurbil, W. Chen, A microstrip transmission line volume coil for human head MR imaging at 4 T, J. Magn. Reson. 161 (2003) 242–251.

[6] P. Sprenger, R.M. Weisskoff, RF gradient quadrature birdcage resonator with improved SNR for functional MRI, in: Annual Meeting of Society of Magnetic Resonance in Medicine, San Francisco, 1994, p. 1104.

[7] E.C. Wong, W.M. Luh, A multimode, single frequency birdcage coil for high sensitivity multichannel whole volume imaging, in: Proceedings of the Seventh Annual Meeting of ISMRM, Philadelphia, 1999, p. 165.

[8] C. Leussler, J. Stimma, P. Röschmann, The bandpass birdcage resonator modified as a coil array for simultaneous MR acquisition, in: Proceedings of the Fifth Annual Meeting of ISMRM, Vancouver, 1997, p. 176.

[9] F.H. Lin, K.K. Kwong, I.J. Huang, J.W. Belliveau, L.L. Wald, Degenerate mode birdcage volume coil for sensitivity encoded imaging, Magn. Reson. Med. 50 (2003) 1107–1111.

[10] K.S. Yee, Numerical solution of initial boundary value problems involving Maxwell equations in isotropic media, IEEE Trans. Ant. Propag. 14 (1966) 302–307.

[11] K.S. Kunz, R.J. Luebbers, The Finite Difference Time Domain Method for Electromagnetics, CRC Press, New York, 1993, p. 448.

[12] Z.P. Liao, H.L. Wong, B. Yang, Y. Yuan, A transmitting boundary for transient wave analysis, Sci. Sin. A 27 (1984) 1063–1076.

[13] C. Gabriel, S. Gabriel, Compilation of the dielectric properties of body tissues at RF and microwave frequencies. Internet document; URL: <www.brooks.af.mil/AFRL/HED/hedr/reports/dielectric/home.html>.

[14] C.M. Collins, S. Li, M.B. Smith, SAR and B_1 field distributions in a heterogeneous human head model within a birdcage coil, Magn. Reson. Med. 40 (1998) 847–856.

[15] M. Alecci, C.M. Collins, M.B. Smith, P. Jezzard, Radio frequency magnetic field mapping of a 3 T birdcage coil: experimental and theoretical dependence on sample properties, Magn. Reson. Med. 46 (2001) 379–385.

[16] D.I. Hoult, The principle of reciprocity in signal strength calculations-A mathematical guide, Concepts Magn. Reson. 12 (4) (2000) 173–187.

[17] M. Weiger, K.P. Prucessmann, C. Leussler, P. Roschmann, P. Boesiger, Specific coil design for SENSE: a six-element cardiac array, Magn. Reson. Med. 45 (2001) 495–504.

[18] P. Kellman, Parallel imaging: the basics, ISMRM Educational Course: MR Physics for Physicists (2004).

[19] P.B. Roemer, W.A. Edelstein, C.E. Hayes, S.P. Souza, O.M. Mueller, The NMR phased array, Magn. Reson. Med. 16 (1990) 192–225.

[20] J.A. Zwart, P.J. Ledden, P. Kellman, P. Gelderen, J.H. Duyn, Design of a SENSE-optimized high-sensitivity MRI receive coil for brain imaging, Magn. Reson. Med. 47 (2002) 1218–1227.

[21] J.V. Hajnal, D.J. Larkman, D.J Herlihy, An array that exploits phase for SENSE imaging, in: Proceedings of the Eighth Annual Meeting of ISMRM, Denver, 2000, p. 1719.